

Redshift Evolution of the Electron Density in the ISM at $z \sim 0 - 9$ Uncovered with JWST/NIRSpec Spectra and Line-Spread Function Determinations

YUKI ISOBE ^{1,2} MASAMI OUCHI ^{3,1,4} KIMHIKO NAKAJIMA ³ YUICHI HARIKANE ¹ YOSHIAKI ONO ¹ YI XU ^{1,5}
YECHI ZHANG,^{1,2} AND HIROYA UMEDA^{1,2}

¹*Institute for Cosmic Ray Research, The University of Tokyo, 5-1-5 Kashiwanoha, Kashiwa, Chiba 277-8582, Japan*

²*Department of Physics, Graduate School of Science, The University of Tokyo, 7-3-1 Hongo, Bunkyo, Tokyo 113-0033, Japan*

³*National Astronomical Observatory of Japan, 2-21-1 Osawa, Mitaka, Tokyo 181-8588, Japan*

⁴*Kavli Institute for the Physics and Mathematics of the Universe (WPI), University of Tokyo, Kashiwa, Chiba 277-8583, Japan*

⁵*Department of Astronomy, Graduate School of Science, The University of Tokyo, 7-3-1 Hongo, Bunkyo, Tokyo 113-0033, Japan*

(Received Jan 17, 2023; Revised Aug 11, 2023; Accepted Aug 22, 2023)

ABSTRACT

We present electron densities n_e in the inter-stellar medium (ISM) of star-forming galaxies at $z = 4 - 9$ observed by the JWST/NIRSpec GLASS, ERO, and CEERS programs. We carefully evaluate line-spread functions of the NIRSpec instrument as a function of wavelength with the calibration data of a planetary nebula taken onboard, and obtain secure [O II] $\lambda\lambda 3726, 3729$ doublet fluxes for 14 galaxies at $z = 4.02 - 8.68$ falling on the star-formation main sequence with the NIRSpec high and medium resolution spectra. We thus derive the electron densities of singly-ionized oxygen nebulae with the standard n_e indicator of [O II] doublet, and find that the electron densities of the $z = 4 - 9$ galaxies are $n_e \gtrsim 300 \text{ cm}^{-3}$ significantly higher than those of low- z galaxies at a given stellar mass, star-formation rate (SFR), and specific SFR. Interestingly, typical electron densities of singly ionized nebulae increase from $z = 0$ to $z = 1 - 3$ and $z = 4 - 9$, which is approximated by the evolutionary relation of $n_e \propto (1+z)^p$ with $p \sim 1 - 2$. Although it is not obvious that the ISM property of n_e is influenced by global galaxy properties, these results may suggest that nebula densities of high- z galaxies are generally high due to the compact morphologies of high- z galaxies evolving by $r_e \propto (1+z)^{-1}$ ($r_{\text{vir}} \propto (1+z)^{-1}$) for a given stellar (halo) mass whose inverse square corresponds to the $p \sim 2$ evolutionary relation. The $p \sim 1 - 2$ evolutionary relation can be explained by a combination of the compact morphology and the reduction of n_e due to the high electron temperature of the high- z metal poor nebulae.

Keywords: Galaxy formation (595); Galaxy structure (622); Star formation (1569); Dwarf galaxies (416)

1. INTRODUCTION

Properties of interstellar medium (ISM) have spectroscopically investigated by many studies using photoionization models (e.g., Nagao et al. 2012; Nakajima & Ouchi 2014; Feltre et al. 2016; Steidel et al. 2016; Sanders et al. 2016a; Schaerer et al. 2018; Kewley et al. 2019; Harikane et al. 2020; Berg et al. 2021; Umeda et al. 2022; Matsumoto et al. 2022). Particularly, electron densities n_e of H II regions are one of the key quantities to describe physical states of ISM. The electron density is usually derived from density-sensitive emission-line ratios such as [O II] $\lambda 3726$ /[O II] $\lambda 3729$, [S II] $\lambda 6716$ /[S II] $\lambda 6731$, and [C III] $\lambda 1907$ /[C III] $\lambda 1909$ (e.g., Kewley et al. 2019). Large spectroscopic surveys have found that star-

forming galaxies with $M_* \sim 10^{10} M_\odot$ have n_e values of low-ionization regions (O II and S II) increasing from $n_e \sim 30$ to $\sim 200 \text{ cm}^{-3}$ with the redshift in the range of $z \sim 0 - 3$ (e.g., Steidel et al. 2014; Shimakawa et al. 2015; Sanders et al. 2016a; Kashino et al. 2017; Davies et al. 2021). Beyond $z \gtrsim 4$, n_e values had not been investigated due to the lack of high-sensitivity near-infrared spectrographs before the arrival of *James Webb Space Telescope* (JWST), except for a few suggestions based on doubly-ionized regions such as $n_e(\text{C III}) \sim 4 - 13 \times 10^4 \text{ cm}^{-3}$ at $z = 10.957$ (Jiang et al. 2021) and $n_e(\text{O III}) \lesssim 500 \text{ cm}^{-3}$ at $z = 7.133$ (Killi et al. 2023). Recently, using the flux ratio of [O III] $\lambda 5007$ from the JWST/NIRSpec Early Release Observations (ERO; Pontoppidan et al. 2022) and [O III] $\lambda 88 \mu\text{m}$ from ALMA observations, Fuji-

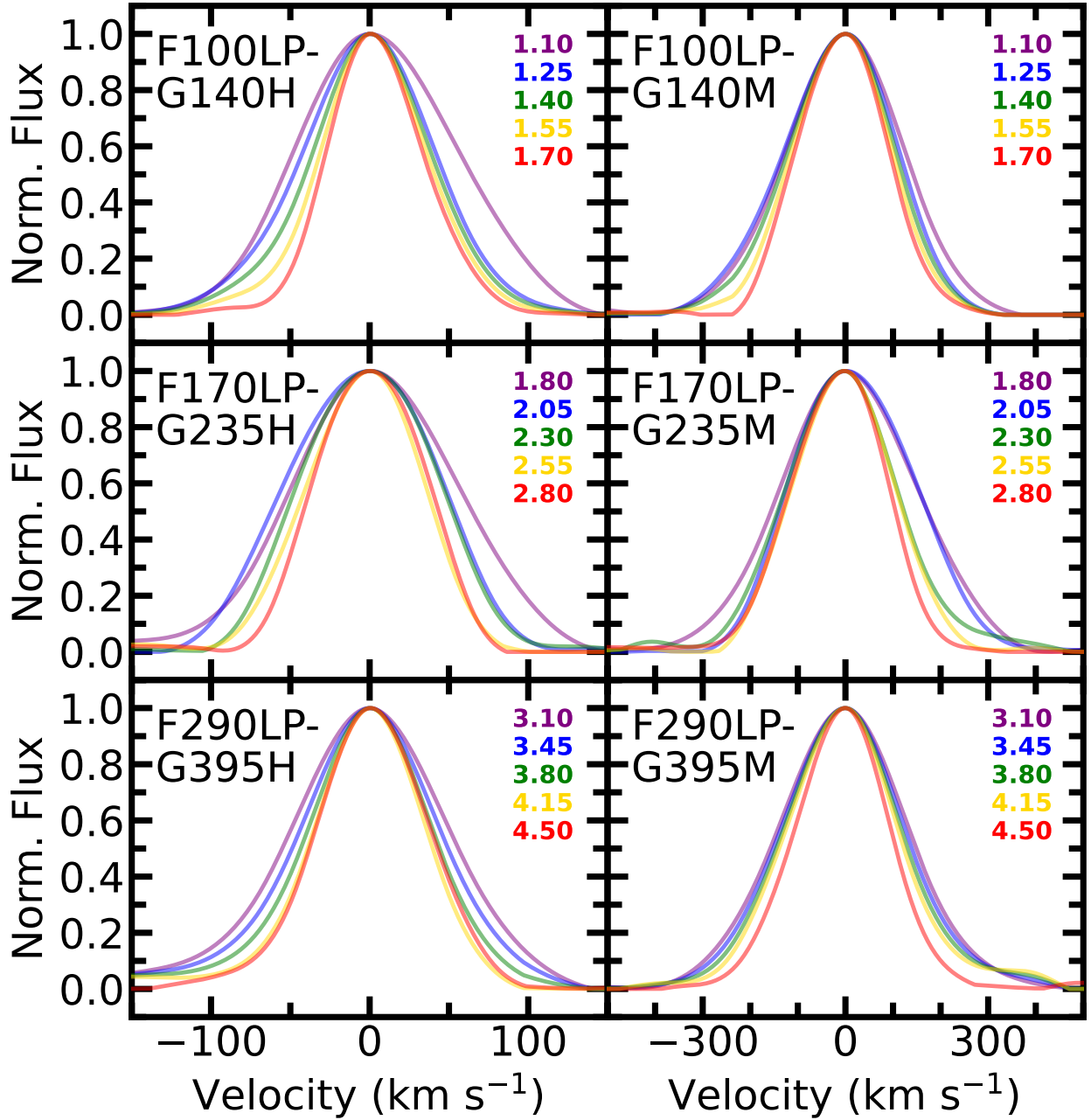


Figure 1. LSF as a function of velocity. In each panel, the purple, blue, green, yellow, and red curves represent LSFs obtained at the wavelengths whose values correspond to the numbers with the same color listed at the top right corner (unit: μm).

[moto et al. \(2022\)](#) have reported that a $z = 8.496$ dwarf galaxy, s04590, has a $n_e(\text{O III})$ value of $220_{-100}^{+170} \text{ cm}^{-3}$.

Although the $n_e(\text{O III}$ or $\text{C III})$ values are likely to be higher than those of $z \sim 0$ star-forming galaxies (e.g., $n_e(\text{O II}) \sim 30 \text{ cm}^{-3}$; [Davies et al. 2021](#)), we need to discuss the redshift evolution of n_e at similar ionization regions (i.e., O II and S II , rather than O III or C III). We should also check if n_e values change with other galaxy

properties such as M_* or star-formation rate (SFR). In this paper, we aim to measure $n_e(\text{O II})$ values of high- z ($z > 4$) star-forming galaxies identified by NIRSspec public surveys. Comparing the n_e values with those of lower- z star-forming galaxies, we also investigate the redshift evolution of n_e and the potential dependences on M_* and SFR.

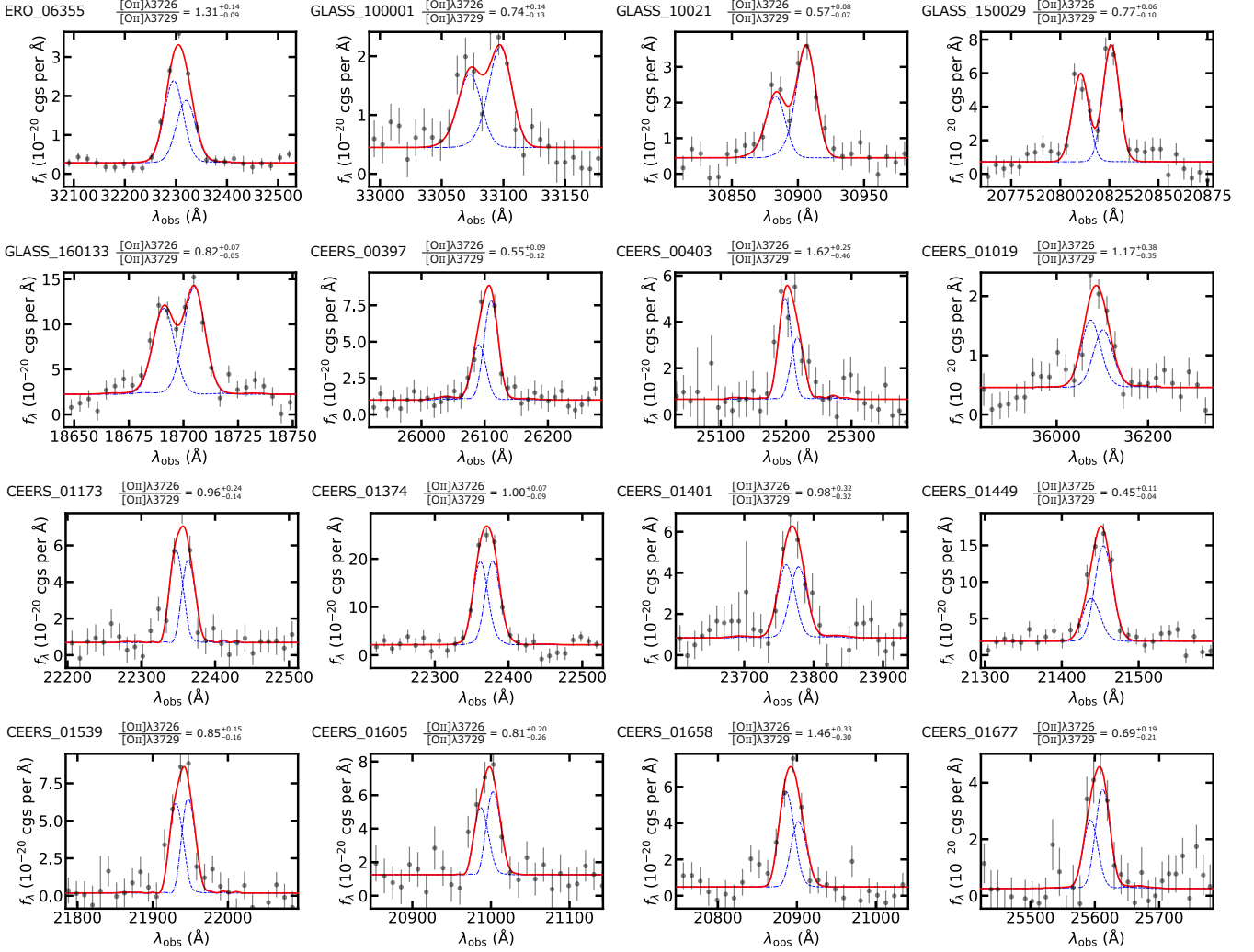


Figure 2. Our fitting results of the LSF-convolved Gaussian functions to the [O II] doublet. The gray dots denote data points with spectral errors. The red solid curve represents a total profile of the [O II] doublet. The blue dashed curve and the blue dashdotted curve show profiles of [O II] λ 3726 and [O II] λ 3729, respectively.

This paper is organized as follows. Section 2 explains our data and sample. Our analysis is described in Section 3. We report our results and discuss them in Section 4. Our findings are summarized in Section 5. We assume a standard Λ CDM cosmology with parameters of $(\Omega_m, \Omega_\Lambda, H_0) = (0.3, 0.7, 70 \text{ km s}^{-1} \text{ Mpc}^{-1})$.

2. DATA AND SAMPLE

We use JWST/NIRSpec data of the Early Release Observations (ERO; Pontoppidan et al. 2022) taken in the SMACS 0723 lensing cluster field (hereafter ERO data), the GLASS (Treu et al. 2022) survey (hereafter GLASS data), and the CEERS (Finkelstein et al. 2023) survey (hereafter CEERS data). The ERO data were taken with medium resolution ($R \sim 1000$) filter-grating pairs of F170LP-G235M and F290LP-G395M covering the wavelength ranges of 1.7–3.1 and 2.9–5.1 μm , re-

spectively. The total exposure time of the ERO data is 4.86 hr for each filter-grating pair. The GLASS data were taken with high resolution ($R \sim 2700$) filter-grating pairs of F100LP-G140H, F170LP-G235H, and F290LP-G395H covering the wavelength ranges of 1.0–1.6, 1.7–3.1 and 2.9–5.1 μm , respectively. The total exposure time of the GLASS data is 4.9 hr for each filter-grating pair. The CEERS data were taken with medium resolution filter-grating pairs of F100LP-G140M, F170LP-G235M, and F290LP-G395M covering the wavelength ranges of 1.0–1.6, 1.7–3.1 and 2.9–5.1 μm , respectively. The total exposure time of the CEERS data is 0.86 hr for each filter-grating pair.

We use spectroscopic data reduced by Nakajima et al. (2023). Nakajima et al. (2023) take the raw data from the MAST archive and conduct level-2 and 3 calibrations, using the JWST Science Calibration Pipeline with

the reference file of `jwst_1028.pmap` whose flux calibration is based on in-flight flat data. In addition to the read-out noise and Poisson noise outputted by the JWST/NIRSpec pipeline, Nakajima et al. (2023) have added standard deviation of the residual background to evaluate the uncertainty of background subtraction. Checking the data, we identify 5, 14, and 55 galaxies at $z > 4$ in the ERO, GLASS, and CEERS data, respectively, whose redshifts by simultaneous fitting of the $H\beta$ and $[\text{O III}]\lambda\lambda 4959, 5007$. We omit galaxies with S/N ratios of the $[\text{O II}]$ doublet less than 10 so that we can obtain galaxies with well-determined n_e . After the selection, we obtain 1, 4, and 11 galaxies from the ERO, GLASS, and CEERS data, respectively. Hereafter we refer to the 16 ($= 1 + 4 + 11$) galaxies as JWST galaxies.

3. ANALYSIS

In this paper, we measure $[\text{O II}]\lambda 3726/[\text{O II}]\lambda 3729$ ratios to obtain $n_e(\text{O II})$. The separation of the observed wavelengths of the $[\text{O II}]\lambda\lambda 3726, 3729$ doublet is even shorter than the double of the expected FWHM of the $R \sim 2700$ grating, which means that the observed $[\text{O II}]$ doublet is not fully deblended even with the $R \sim 2700$ grating. To deblend the $[\text{O II}]$ doublet, we should determine emission-line profiles of observed galaxies using line-spread functions (LSFs) of NIRSpec and intrinsic velocity dispersions (σ_{int}) of the observed galaxies. Section 3.1 describes how we derive the LSFs, and Section 3.2 explains how we measure σ_{int} .

3.1. Line-Spread Function

We obtain the LSFs from a planetary nebula (PN), IRAS-05248-7007. NIRSpec spectra of the PN were taken during the commissioning process (proposal ID: 1125). The PN was observed with a slit whose width is 0.2 arcsec, which is the same as those of the MSA shutters. We use the level-3 spectra available at MAST. We choose emission lines with high S/N ratios. We also avoid using emission lines blended with other nearby features. After the selection, we obtain 4, 11, 5 emission lines for the spectra obtained with the filters F100LP, F170LP, and F290LP, respectively. The selected emission lines cover wide wavelength ranges of 1.1–1.7, 1.8–2.8, and 3.1–4.5 μm for the filters F100LP, F170LP, and F290LP, respectively. To obtain the LSF at an arbitrary wavelength, we interpolate the LSF profiles.

Figure 1 summarizes LSFs at different wavelengths for each filter-grating pair. The obtained LSFs of F100LP-G140H, F170LP-G235H, F290LP-G395H, F100LP-G140M, F170LP-G235M, and F290LP-G395M have median resolution values of $R \simeq 3180, 2800, 3390, 1160, 1120, \text{ and } 1080$ obtained in wavelength ranges of

1.1–1.7, 1.8–2.8, 3.1–4.5, 1.1–1.7, 1.8–2.8, and 3.1–4.5 μm , respectively. These resolution values are ~ 10 – 20% larger than those of the nominal resolutions of $R \sim 2700$ for the high-resolution gratings and $R \sim 1000$ for the medium-resolution gratings. We also confirm that LSFs of each filter-grating pair become narrower (i.e., better resolution) with longer wavelengths, which is also expected by the NIRSpec instrumental team¹.

The PN was also observed by VLT/X-shooter with the spectral resolution of $R \sim 6500$ (Euclid Collaboration et al. 2023; the spectral properties are available in the Visier atlas²). The observed line widths of the PN are nearly the same as those expected from the spectral resolution of 6500, which suggests that the PN's bulk motions are not resolved with $R \sim 6500$. This also indicates that NIRSpec cannot resolve the PN's bulk motions with the NIRSpec spectral resolution of ~ 1000 or ~ 2700 .

Nevertheless, the PN may have unresolved bulk motions. Given that intrinsic velocity dispersions (σ_{int}) of PNe are typically $\sim 30 \text{ km s}^{-1}$ (Jacob et al. 2013), we may not be able to measure σ_{int} values of galaxies with $\sigma_{\text{int}} \lesssim 30 \text{ km s}^{-1}$. To put it the other way around, the σ_{int} value of 30 km s^{-1} does not change the LSF profiles largely, i.e., the σ_{int} accounts for only $\sim 1\%$ and $\sim 8\%$ of the observed velocity dispersion of the PN with the $R \sim 1000$ and ~ 2700 gratings, respectively.

3.2. Velocity-Dispersion Measurement

To obtain σ_{int} of the observed galaxies, we fit a Gaussian function convolved with the LSF derived in Section 3.1. To obtain σ_{int} with smaller uncertainties, we measure σ_{int} of $[\text{O III}]\lambda 5007$, which is the strongest in the observed emission lines. We conduct the fittings to $[\text{O III}]\lambda\lambda 4959, 5007$ simultaneously so that line profiles of the two emission lines are reproduced self-consistently. We fix the flux ratio $[\text{O III}]\lambda 5007/[\text{O III}]\lambda 4959$ to 2.98, which is accurately determined by the Einstein A coefficient (Storey & Zeippen 2000).

We note that our fitting provides $\sigma_{\text{int}} \sim 0 \text{ km s}^{-1}$ for 2 of the 16 JWST galaxies (CEERS_01173 and CEERS_01539). We adopt $\sigma_{\text{int}} = 0 \text{ km s}^{-1}$ for the 2 JWST galaxies to determine $[\text{O II}]$ -doublet profiles, while true σ_{int} values of the 2 JWST galaxies are likely to be larger than 0 km s^{-1} and less than that of the

¹ <https://jwst-docs.stsci.edu/jwst-near-infrared-spectrograph/nirspec-instrumentation/nirspec-dispersers-and-filters>

² http://vizier.cfa.harvard.edu/viz-bin/VizieR-3?-source=J/A%2bA/674/A172/pn-0-11&-out.max=50&-out.form=HTML%20Table&-out.add=_r&-out.add=_RAJ,_DEJ&-sort=_r&-oc.form=sex

Table 1. Electron density and other properties

Name	R.A.	Decl.	z	$n_e(\text{O II})$	$\frac{[\text{O II}]\lambda 3726}{[\text{O II}]\lambda 3729}$	σ_{int}	$\log(M_*)$	$\log(\text{SFR})$
(1)	deg	deg	(4)	cm^{-3}	(6)	km s^{-1}	M_\odot	$M_\odot \text{ yr}^{-1}$
(1)	(2)	(3)	(4)	(5)	(6)	(7)	(8)	(9)
ERO_06355	110.8267392	-73.4537444	7.6651	1433^{+752}_{-335}	$1.31^{+0.14}_{-0.09}$	113	$8.77^{+0.08}_{-0.01}$ ^a	$1.41^{+0.01}_{-0.01}$ ^a
GLASS_100001	3.6038450	-30.3822350	7.8737	118^{+217}_{-118}	$0.74^{+0.14}_{-0.13}$	69	$9.15^{+0.55}_{-0.00}$ ^a	$0.95^{+0.10}_{-0.13}$ ^a
GLASS_150029	3.5771664	-30.4225760	4.5837	174^{+137}_{-174}	$0.77^{+0.06}_{-0.10}$	38	$9.12^{+0.03}_{-0.33}$ ^a	$1.04^{+0.02}_{-0.02}$ ^a
GLASS_160133	3.5802754	-30.4244040	4.0150	252^{+161}_{-103}	$0.82^{+0.07}_{-0.05}$	59	$8.11^{+0.41}_{-0.22}$ ^a	$1.16^{+0.01}_{-0.01}$ ^a
CEERS_00397	214.8361970	52.8826930	6.0005	0^{+1}_{-0}	$0.55^{+0.09}_{-0.12}$	81	$8.45^{+0.53}_{-0.06}$ ^a	$1.76^{+0.02}_{-0.03}$ ^a
CEERS_00403	214.8289680	52.8757010	5.7609	3105^{+3232}_{-2151}	$1.62^{+0.25}_{-0.46}$	56	$9.35^{+0.27}_{-0.09}$ ^a	$1.20^{+0.06}_{-0.07}$ ^a
CEERS_01019	215.0353914	52.8906618	8.6791	1118^{+3332}_{-969}	$1.17^{+0.38}_{-0.35}$	123	$10.12^{+0.12}_{-0.11}$ ^a	$1.97^{+0.04}_{-0.05}$ ^a
CEERS_01173	215.1542076	52.9558470	4.9957	574^{+942}_{-331}	$0.96^{+0.24}_{-0.14}$... ^c	$9.38^{+1.12}_{-1.12}$ ^b	$0.56^{+0.13}_{-0.13}$ ^b
CEERS_01374	214.9439110	52.8500419	4.9999	656^{+254}_{-219}	$1.00^{+0.07}_{-0.09}$	67	$9.44^{+1.12}_{-1.12}$ ^b	$1.36^{+0.03}_{-0.03}$ ^b
CEERS_01401	215.2458005	53.0652953	5.3749	613^{+1934}_{-613}	$0.98^{+0.32}_{-0.32}$	112	< 8.92 ^b	$0.86^{+0.09}_{-0.09}$ ^b
CEERS_01539	214.9800779	52.9426590	4.8841	330^{+444}_{-327}	$0.85^{+0.15}_{-0.16}$... ^c	< 8.71 ^b	$0.80^{+0.05}_{-0.05}$ ^b
CEERS_01605	215.0754073	52.9975786	4.6309	250^{+537}_{-250}	$0.81^{+0.20}_{-0.26}$	16	$9.11^{+1.10}_{-1.10}$ ^b	$0.53^{+0.06}_{-0.06}$ ^b
CEERS_01658	214.9852372	52.9242590	4.6038	2199^{+5950}_{-1078}	$1.46^{+0.33}_{-0.30}$	64	< 8.56 ^b	$0.67^{+0.06}_{-0.06}$ ^b
CEERS_01677	215.1887384	53.0643782	5.8670	39^{+470}_{-39}	$0.69^{+0.19}_{-0.21}$	83	$9.07^{+0.84}_{-0.84}$ ^b	$0.69^{+0.08}_{-0.08}$ ^b

NOTE—(1) Name. (2) Right ascension in J2000. (3) Declination in J2000. (4) Redshift. (5) Electron density derived from the [O II] doublet (Section 3.3). (6) Velocity dispersion (Section 3.2). (7) Stellar mass (Section 3.4). (8) Star-formation rate (Section 3.4).

a: The M_* and SFR values are estimated from SED fitting to JWST/NIRCam photometry with prospector (Johnson et al. 2021) and $H\beta$ fluxes corrected for slit losses, respectively (Nakajima et al. 2023; Section 3.4).

b: The M_* and SFR values are estimated from HST restframe-UV photometry and $H\beta$ fluxes not corrected for slit losses, respectively, because no NIRCam photometry are available for these objects to date (Section 3.4).

c: The σ_{int} values are too small to measure (Sections 3.1 and 3.2).

PN used for the LSFs (i.e., $0 < \sigma_{\text{int,true}} \lesssim 30 \text{ km s}^{-1}$; Section 3.1).

3.3. Electron-Density Measurement

Using the LSF (Section 3.1), we measure fluxes of the [O II] doublet. We fit 3 Gaussian functions convolved by the LSF to [O II] $\lambda\lambda 3726, 3729$, and [O III] $\lambda 5007$ simultaneously with the fixed z . Figure 2 shows our fitting results. We use PyNeb (Luridiana et al. 2015; v1.1.15) to obtain n_e from the [O II] doublet. This method provides n_e values consistent with those derived from the updated relation between [O II] $\lambda 3729$ /[O II] $\lambda 3726$ and n_e reported by Sanders et al. (2016a). In ERO_06355, GLASS_150029, GLASS_160133, and CEERS_00397, electron temperatures of 11300, 17600, 14800, and 15200 K, respectively, have been measured from the [O III] $\lambda 4363$ line (Nakajima et al. 2023; Isobe et al. 2023). For these 4 galaxies, we use these temperature values when deriving the n_e values. For the other galaxies, we assume electron temperatures of the JWST galaxies to be 15000 K, which is typical for star-forming dwarf galaxies (e.g., Izotov et al. 2012; Kojima et al. 2020; Isobe et al. 2022; Nakajima et al. 2022). We perform

Monte Carlo simulations based on spectral errors to obtain uncertainties of n_e . We note that 2 of the 16 JWST galaxies (GLASS_10021 and CEERS_01449) show unphysical [O II] $\lambda 3726$ /[O II] $\lambda 3729$ ratios, even including the spectral errors into the n_e measurements. Omitting the 2 galaxies, we obtain a final sample consisting of 14 (= 16 - 2) galaxies. Table 1 lists the derived n_e with the uncertainties.

Since the n_e values based on the $R \sim 2700$ observations are slightly lower than those with $R \sim 1000$, we have performed a recovery test for the $R \sim 1000$ data by making mock spectra around the [O II] $\lambda\lambda 3726, 3729$ and [O III] $\lambda 5007$ lines with a typical σ_{int} of 60 km s^{-1} convolved by the LSFs and noises that match typical S/N ratios of these line fluxes. Conducting line fitting to the mock spectra in the same way as for the scientific data, we have confirmed that our fitting method can reproduce electron density values within at most 3.5% accuracy even for the $R \sim 1000$ spectra.

We check that different assumptions of electron temperatures from $T_e = 10000$ to 30000 K can change n_e values by at most $\sim 20\%$ from those calculated by the original assumption of $T_e = 15000$ K. This systemat-

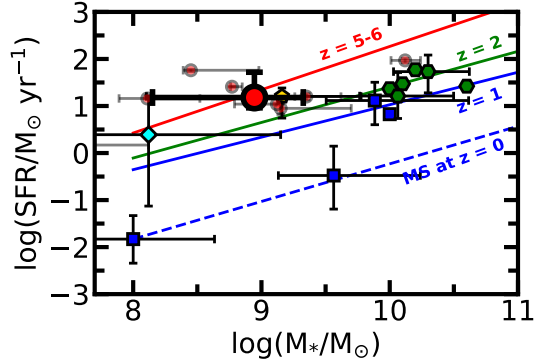


Figure 3. M_* -SFR relation of the JWST galaxies with the NIRCcam photometry at $4 < z < 9$ represented by the red circles. We also plot median n_e values of star-formation main-sequence (SFMS) galaxies with $M_* \sim 10^8$ - $10^{10} M_\odot$ at $z \sim 0$ -1 (blue square; [O II]- or [S II]-based; Berg et al. 2012; Davies et al. 2021; Swinbank et al. 2019) and with $M_* \sim 10^{10} M_\odot$ at $z \sim 1$ -3 (green hexagon; [O II]- or [S II]-based; Davies et al. 2021; Kaasinen et al. 2017; Kashino et al. 2017; Sanders et al. 2016a; Steidel et al. 2014). The red solid, green solid, blue solid, and blue dashed lines illustrate SFMSs at $z = 5$ -6 (Santini et al. 2017), $z = 2$ (Speagle et al. 2014), $z = 1$ (Speagle et al. 2014) and $z = 0$ (Chang et al. 2015), respectively. We also show median n_e values of high SFR galaxies with $M_* \sim 10^8 M_\odot$ at $z \sim 0$ (cyan diamond; [S II]-based; Berg et al. 2022) and with $M_* \sim 10^9 M_\odot$ at $z \sim 2$ -3 (yellow pentagon; [O II]-based; Christensen et al. 2012a,b; Sanders et al. 2016b; Gburek et al. 2019).

ics of n_e is much smaller than those derived from the spectral errors.

3.4. M_* and SFR

In this paper, we characterize the JWST galaxies with their M_* and SFR values. Seven of the 14 JWST galaxies have JWST/NIRCcam photometry at the time of writing. Regarding these 6 galaxies, we use M_* and SFR values derived by Nakajima et al. (2023). Nakajima et al. (2023) derive M_* by conducting SED fitting with prospector (Johnson et al. 2021) assuming the Chabrier (2003) IMF, a flexible star formation history, and the Calzetti et al. (2000) dust extinction law, in a similar manner to Harikane et al. (2023). NIRCcam photometries of the JWST galaxies are measured by Source Extractor (Bertin & Arnouts 1996) as in Harikane et al. (2023). The photometries are corrected for gravitational lensing magnifications modeled by glafic (Oguri 2010). We then correct the NIRSpc spectra for slit losses by scaling the spectra to match the NIRCcam photometries, where the typical correction factor is about 1.3. The SFR values are calculated from slitloss-corrected $H\beta$ luminosities with the NIRCcam restframe optical photometry under the assumptions of the Kennicutt (1998) rela-

tion and Chabrier (2003) IMF. Figure 3 shows M_* -SFR relations of the JWST galaxies with the NIRCcam photometry. The median M_* and SFR values of the JWST galaxies (large red circle) show that the JWST galaxies generally lie on the star-formation main sequence (SFMS) at $z = 5$ -6 (Santini et al. 2017).

We estimate M_* of the remaining 7 ($= 14 - 7$) JWST galaxies from broadband photometry of HST/ACS F606W, F814W, or HST/WFC3 F125W taken from the CANDELS EGS catalog (Stefanon et al. 2017). We use FLUX_AUTO values based on Source Extractor (Bertin & Arnouts 1996) as total fluxes. Assuming that the 7 JWST galaxies lie on the SFMS as well as the 7 JWST galaxies with the NIRCcam photometry, we adopt empirical relations between M_* and absolute magnitude of restframe 1500 \AA (M_{UV}) derived at $z = 4, 5, 6, 7,$ and 8 (Song et al. 2016; based on the Salpeter 1955 IMF). We choose the M_* - M_{UV} relation and the HST photometry both consistent with the redshift of each JWST galaxy. Note that 3 of the 7 JWST galaxies do not have $> 5\sigma$ detection of HST photometry. For these 3 JWST galaxies, we calculate upper limits of M_* based on 5σ limiting magnitudes of the HST photometry. For consistency with M_* values derived by Nakajima et al. (2023), we rescale the M_* values from the Salpeter (1955) to Chabrier (2003) IMF by multiplying 0.61 (Madau & Dickinson 2014). We check that the M_* values based on the HST photometry are consistent with those of Nakajima et al. (2023) within a 1σ level. We have propagated errors of the HST photometry and the M_* - M_{UV} relations to the final stellar mass errors. The scatters of the M_* - M_{UV} relations are ~ 0.15 dex at $z \sim 4$ and ~ 0.3 dex at $z \sim 8$, which are smaller than those of our derived stellar mass errors. This indicates that the stellar mass errors are dominated by the HST photometry.

We also calculate SFRs of the 7 JWST galaxies from $H\beta$ luminosities under the assumptions of the Kennicutt (1998) relation and Chabrier (2003) IMF in the same manner as Nakajima et al. (2023). Although we do not correct the $H\beta$ luminosities of these 7 galaxies without the NIRCcam photometry for slit losses, the small typical slit-loss correction factor of 1.3 suggests that the slit-loss correction does not change the SFR values much. We summarize the M_* and SFR values in Table 1.

4. RESULT AND DISCUSSION

Figure 4 presents n_e - M_* (left), $-\text{SFR}$ (center), and $-\text{sSFR}$ (right) relations. The small red circles and the small red double circle in Figure 4 represent the properties of each JWST galaxy at $z \sim 4$ -6 and $z \sim 7$ -9, respectively. The large red circles and the large red double circles denote median and 16th-84th percentiles of the

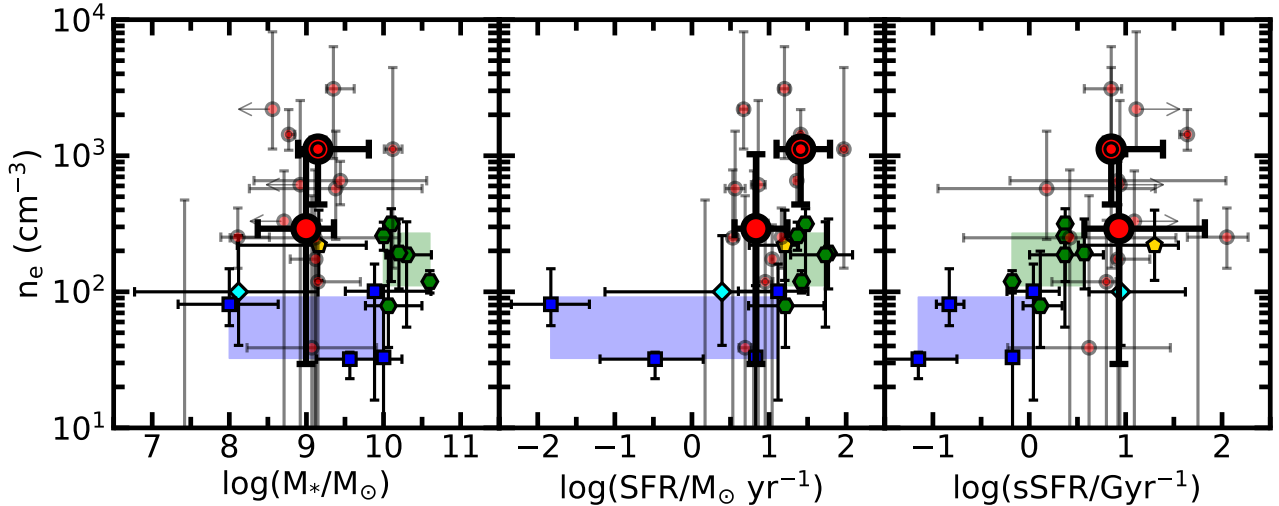


Figure 4. Electron density n_e as a function of M_* (left), SFR (center), and sSFR (right). The large red circles and the large red double circles denote median and 16th-84th percentiles of the properties of the JWST galaxies at $z \sim 4-6$ and $z \sim 7-9$, respectively. The small red circles and the small red double circle represent the properties of each JWST galaxy at $z \sim 4-6$ and $z \sim 7-9$, respectively. The other symbols are the same as those in Figure 3. The blue and green shaded regions correspond to the 16th-84th percentile ranges of the n_e values of the galaxies at $z \sim 0-1$ (Berg et al. 2012; Davies et al. 2021; Swinbank et al. 2019) and $z \sim 1-3$ (Davies et al. 2021; Kaasinen et al. 2017; Kashino et al. 2017; Sanders et al. 2016a; Steidel et al. 2014), respectively. On average, the JWST galaxies have higher n_e than those of lower- z galaxies at a given M_* , SFR, and sSFR.

properties of the JWST galaxies at $z \sim 4-6$ and $z \sim 7-9$, respectively. We find that the median n_e values of the JWST galaxies at $z \sim 4-6$ and $z \sim 7-9$ are ~ 300 and $\sim 1000 \text{ cm}^{-3}$, respectively.

For comparison, we compile median n_e values of SFMS galaxies at $z \sim 0-1$ (blue square; Berg et al. 2012; Davies et al. 2021; Swinbank et al. 2019) and $z \sim 1-3$ (green hexagon; [O II]- or [S II]-based; Davies et al. 2021; Kaasinen et al. 2017; Kashino et al. 2017; Sanders et al. 2016a; Steidel et al. 2014) whose M_* -SFR relations are shown in Figure 3. We note that we derive the median n_e value of Berg et al. (2012) from the flux ratios of [S II] $\lambda 6716$ /[S II] $\lambda 6731$ and T_e of 31 galaxies in Berg et al. (2012). In addition, the median SFR values of Davies et al. (2021) are read from their figures.

It should be noted that n_e values are reported not to be very dependent on M_* (Kashino & Inoue 2019) but on SFR and sSFR (e.g., Shimakawa et al. 2015; Jiang et al. 2019; Kashino & Inoue 2019; Davies et al. 2021) at a given redshift. To examine how much the n_e values change with SFR and sSFR, we plot the 16th-84th percentile ranges of the n_e values of the SFMS galaxies at $z \sim 0-1$ with the blue shaded region and at $z \sim 1-3$ with the green shaded region, respectively, in Figure 4. The blue shaded region indicates that the

n_e dependencies on M_* , SFR, and sSFR in the ranges of $\log(M_*/M_\odot) \sim 8-10$, $\log(\text{SFR}/M_\odot \text{ yr}^{-1}) \sim -2-1$, and $\log(\text{sSFR}/\text{Gyr}^{-1}) \sim -1-0$, respectively, are folded in the n_e range of $\sim 30-100 \text{ cm}^{-3}$. Note that the sSFR values of the SFMS galaxies at $z \sim 0-1$ are lower than those of the JWST galaxies. The SFMS galaxies at $z \sim 1-3$ typically have $n_e \sim 100-300$, while the parametric ranges examined are relatively narrow, i.e., $\log(M_*/M_\odot) \sim 10-10.5$, $\log(\text{SFR}/M_\odot \text{ yr}^{-1}) \sim 1-2$, and $\log(\text{sSFR}/\text{Gyr}^{-1}) \sim 0-0.5$.

To cover higher sSFRs that match those of the JWST galaxies, we also refer to active star-forming galaxies at $z \sim 0$ (cyan diamond; Berg et al. 2022) and $\sim 2-3$ (yellow pentagon; Christensen et al. 2012a,b; Sanders et al. 2016b; Gburek et al. 2019) whose sSFR values are comparable to those of the JWST galaxies (cf. Figure 3). We refer to these galaxies as high sSFR galaxies. The median values of the high sSFR galaxies at $z \sim 0$ and $z \sim 2-3$ are ~ 100 and $\sim 200 \text{ cm}^{-3}$, respectively, both of which are comparable to those of the SFMS galaxies at a given redshift.

The left and center panels of Figure 4 illustrate that the n_e values increase from the $z \sim 0-1$ to $z \sim 1-3$ and $z \sim 4-9$ at a given M_* and SFR. This indicates that n_e evolves with redshift beyond the range that can be

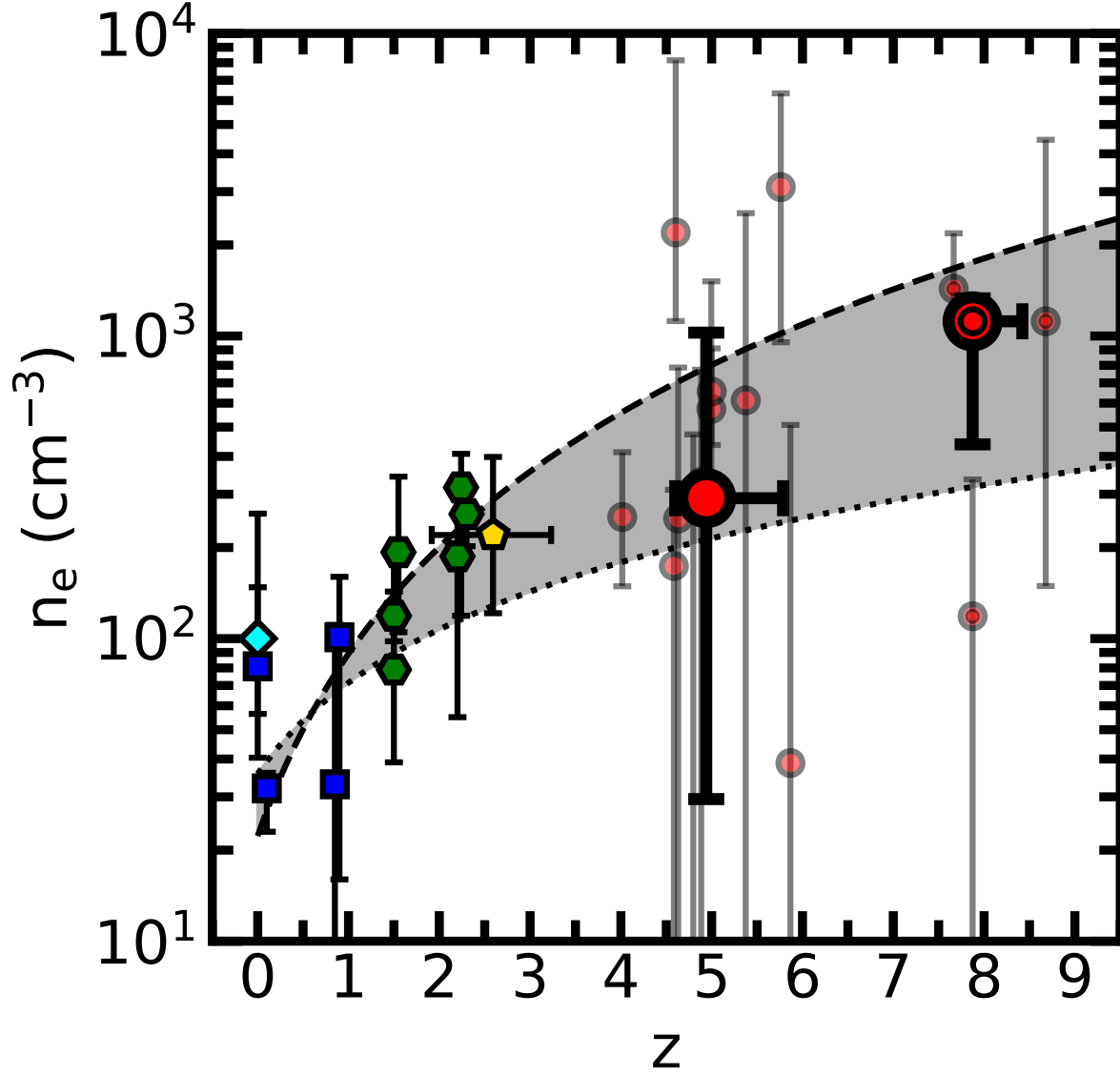


Figure 5. Electron density n_e as a function of redshift. All of the measurements in this figure are based on the low-ionization lines (i.e., [O II] or [S II]). The symbols are the same as those in Figure 4. The dotted and dashed curves represent n_e following $\propto (1+z)$ and $\propto (1+z)^2$ relations, respectively, which are determined by the galaxies at $z \sim 0-3$. The JWST galaxies lie on the gap between the two functions (i.e., $n_e \propto (1+z)$ and $\propto (1+z)^2$) filled with the gray shaded region.

explained by the correlation of n_e and SFR. On the other hand, the sSFR distribution of the JWST galaxies does not overlap with that of the SFMS galaxies at $z \sim 0-3$ as shown in the right panel of Figure 4, which makes it hard to tell if the n_e values evolve with redshift or correlate with sSFR. However, compared with the high sSFR galaxies at $z \sim 0$ (cyan diamond) and $z \sim 2-3$ (yellow pentagon), the n_e values are likely to increase from the $z \sim 0-1$ to $z \sim 1-3$ and $z \sim 4-9$ at a given sSFR as well. Note that the $z \sim 0$ high sSFR sample consists of 45 galaxies, comparable to those of Davies et al. (2021) in each redshift bin, while the $z \sim 2-3$ high sSFR sample consists of only 5 galaxies due to the lack of statistical surveys for $z \sim 2-3$ dwarf galaxies.

Figure 5 clearly shows that the n_e values typically increase from $z \sim 0$ to $z \sim 1-3$ and $z \sim 4-9$. We then investigate the dependence of n_e on z by comparing the n_e values of the JWST galaxies with an extrapolation of the increasing trend identified in lower- z galaxies. Assuming that the lower- z galaxies follow $n_e \propto (1+z)$ or $\propto (1+z)^2$ relation, we fit the 2 functions to the $z \sim 0-3$ galaxies based on χ^2 minimization. We find that the JWST galaxies at $z \sim 4-9$ have median n_e and z values (large red circles) falling in the gap between the $n_e \propto (1+z)$ and $\propto (1+z)^2$ relations (gray shaded region), which suggests that galaxies at $z \sim 0-9$ have an evolutionary relation of $n_e \propto (1+z)^p$ with $p \sim 1-2$.

Although it is not obvious that global galaxy properties impact on the ISM property of n_e , the $n_e \propto (1+z)^2$ relation suggests that nebula densities of high- z star-forming galaxies are generally high due to the compact morphology, i.e., smaller effective radii r_e and virial radii r_{vir} . Given the size evolutions of $r_e \propto (1+z)^{-1}$ (Shibuya et al. 2015; Ono et al. 2023) and $r_{\text{vir}} \propto (1+z)^{-1}$ (e.g., Mo & White 2002), stellar- and halo-mass densities are expected to be proportional to $r_e^{-2} \propto (1+z)^2$ and $r_{\text{vir}}^{-2} \propto (1+z)^2$ at a given mass, respectively, under the assumption that star-forming galaxies have disks (suggested by their low Sérsic indices; cf. Shibuya et al. 2015; Ono et al. 2023) whose heights are constant. If the stellar-mass and halo-mass densities are proportional to n_e , n_e is approximately proportional to $(1+z)^2$. This suggestion is similar to the conclusion claimed by Davies et al. (2021).

However, the JWST galaxies generally have n_e values slightly lower than those predicted by the $p = 2$ evolutionary relation. Although this discrepancy may be explained by the $\sim 20\%$ uncertainty of the electron temperature (Section 3.3), we should think of other factors that can decrease n_e values. One possible explanation is that thermal expansions at higher electron temperatures of high- z metal-poor nebulae result in lower n_e

values for a given pressure (Kewley et al. 2019). The $p \sim 1-2$ evolutionary relation of n_e may originate from a combination of the compact morphology and the high electron temperature of high- z galaxies. It should be noted that the JWST galaxies have M_* values ~ 1 dex smaller than those of the SFMS galaxies at $z \sim 0-3$. Since the observed size-mass relation is a positive trend, $z \sim 0-3$ galaxies with similar M_* to the JWST galaxies may have larger n_e values than the current SFMS samples. This could lead to an even flatter redshift evolution of n_e .

It should also be noted that there is a possibility that the relatively-high S/N criterion for the [O II] doublet (Section 2) causes a bias towards lower [O III] λ 5007/[O II] $\lambda\lambda$ 3727,3729 ratios (O32, hereafter). This potential bias leads to ionization parameters q lower (e.g., Kewley & Dopita 2002), which leads to high n_e evidenced with $q \propto n_{\text{H}}^{-1}$, where n_{H} is a hydrogen number density roughly proportional to n_e . However, the JWST galaxies already have a high median O32 value of $\simeq 5$, which indicates that the JWST galaxies are not biased towards low O32.

5. SUMMARY

We present electron densities of singly-ionized regions $n_e(\text{O II})$ in the inter-stellar medium (ISM) of star-formation main-sequence galaxies at $z = 4-9$ observed by JWST/NIRSpec ERO, GLASS, and CEERS programs. Deriving line-spread functions of the NIRSpec instrument from in-flight calibration data, we securely measure [O II] λ 3726/[O II] λ 3729 ratios of 14 galaxies at $z = 4.02-8.68$. We find that the 14 galaxies have $n_e \gtrsim 300 \text{ cm}^{-3}$ significantly higher than those of low- z galaxies at a given stellar mass, star-formation rate (SFR), and specific SFR (Figure 4). We also identify an increase in typical n_e values from $z = 0$ to $z = 1-3$ and $z = 4-9$, which is approximated by $n_e \propto (1+z)^p$ with $p \sim 1-2$ (Figure 5). Although it is not obvious that the ISM property of n_e is influenced by global galaxy properties, the $p \sim 1-2$ evolutionary relation can be explained by a combination of the compact morphology and the reduction of n_e due to high electron temperatures of high- z metal-poor nebulae.

We thank M. Oguri for providing his lens models. We also thank H. Yajima and H. Fukushima for having useful discussions. We are grateful to staff of the James Webb Space Telescope Help Desk for letting us know useful information. This work is based on observations made with the NASA/ESA/CSA James Webb Space Telescope. Some of the data presented in this paper were obtained from the Mikulski Archive for Space Telescopes

(MAST) at the Space Telescope Science Institute, which is operated by the Association of Universities for Research in Astronomy, Inc., under NASA contract NAS 5-03127 for JWST. The specific observations analyzed can be accessed via [10.17909/qfxm-y747](https://doi.org/10.17909/qfxm-y747). These observations are associated with programs 1125, 2736, 1324, and 1345. The authors acknowledge the ERO, GLASS, and CEERS teams led by Klaus M. Pontoppidan, Tommaso Treu, and Steven L. Finkelstein, respectively, for developing their observing programs with a zero-exclusive-access period. This work is based on observations taken by the CANDELS Multi-Cycle Treasury Program with the NASA/ESA HST, which is operated by the Association of Universities for Research in Astronomy, Inc., under NASA contract NAS5-26555. This work was supported by the joint research program of the Institute

for Cosmic Ray Research (ICRR), University of Tokyo. Y.I., K.N., and Y.H. are supported by JSPS KAKENHI Grant Nos. 21J20785, 20K22373, and 21K13953, respectively. This paper is supported by World Premier International Research Center Initiative (WPI Initiative), MEXT, Japan, as well as the joint research program of the Institute of Cosmic Ray Research (ICRR), the University of Tokyo. This work is supported by KAKENHI (19H00697, 20H00180, and 21H04467) Grant-in-Aid for Scientific Research (A) through the Japan Society for the Promotion of Science. This research was supported by a grant from the Hayakawa Satio Fund awarded by the Astronomical Society of Japan.

Software: astropy (Astropy Collaboration et al. 2013; The Astropy Collaboration 2018), PyNeb (Luridiana et al. 2015), prospector (Johnson et al. 2021), glafic (Oguri 2010), Source Extractor (Bertin & Arnouts 1996)

REFERENCES

- Astropy Collaboration, Robitaille, T. P., Tollerud, E. J., et al. 2013, *A&A*, 558, A33, doi: [10.1051/0004-6361/201322068](https://doi.org/10.1051/0004-6361/201322068)
- Berg, D. A., Chisholm, J., Erb, D. K., et al. 2021, *ApJ*, 922, 170, doi: [10.3847/1538-4357/ac141b](https://doi.org/10.3847/1538-4357/ac141b)
- Berg, D. A., Skillman, E. D., Marble, A. R., et al. 2012, *ApJ*, 754, 98, doi: [10.1088/0004-637X/754/2/98](https://doi.org/10.1088/0004-637X/754/2/98)
- Berg, D. A., James, B. L., King, T., et al. 2022, *ApJS*, 261, 31, doi: [10.3847/1538-4365/ac6c03](https://doi.org/10.3847/1538-4365/ac6c03)
- Bertin, E., & Arnouts, S. 1996, *A&AS*, 117, 393, doi: [10.1051/aas:1996164](https://doi.org/10.1051/aas:1996164)
- Calzetti, D., Armus, L., Bohlin, R. C., et al. 2000, *ApJ*, 533, 682, doi: [10.1086/308692](https://doi.org/10.1086/308692)
- Chabrier, G. 2003, *PASP*, 115, 763, doi: [10.1086/376392](https://doi.org/10.1086/376392)
- Chang, Y.-Y., van der Wel, A., da Cunha, E., & Rix, H.-W. 2015, *ApJS*, 219, 8, doi: [10.1088/0067-0049/219/1/8](https://doi.org/10.1088/0067-0049/219/1/8)
- Christensen, L., Richard, J., Hjorth, J., et al. 2012a, *MNRAS*, 427, 1953, doi: [10.1111/j.1365-2966.2012.22006.x](https://doi.org/10.1111/j.1365-2966.2012.22006.x)
- Christensen, L., Laursen, P., Richard, J., et al. 2012b, *MNRAS*, 427, 1973, doi: [10.1111/j.1365-2966.2012.22007.x](https://doi.org/10.1111/j.1365-2966.2012.22007.x)
- Davies, R. L., Förster Schreiber, N. M., Genzel, R., et al. 2021, *ApJ*, 909, 78, doi: [10.3847/1538-4357/abd551](https://doi.org/10.3847/1538-4357/abd551)
- Euclid Collaboration, Paterson, K., Schirmer, M., et al. 2023, *A&A*, 674, A172, doi: [10.1051/0004-6361/202346252](https://doi.org/10.1051/0004-6361/202346252)
- Feltre, A., Charlot, S., & Gutkin, J. 2016, *MNRAS*, 456, 3354, doi: [10.1093/mnras/stv2794](https://doi.org/10.1093/mnras/stv2794)
- Finkelstein, S. L., Bagley, M. B., Ferguson, H. C., et al. 2023, *ApJL*, 946, L13, doi: [10.3847/2041-8213/acade4](https://doi.org/10.3847/2041-8213/acade4)
- Fujimoto, S., Ouchi, M., Nakajima, K., et al. 2022, arXiv e-prints, arXiv:2212.06863, <https://arxiv.org/abs/2212.06863>
- Gburek, T., Siana, B., Alavi, A., et al. 2019, *ApJ*, 887, 168, doi: [10.3847/1538-4357/ab5713](https://doi.org/10.3847/1538-4357/ab5713)
- Harikane, Y., Ouchi, M., Inoue, A. K., et al. 2020, *ApJ*, 896, 93, doi: [10.3847/1538-4357/ab94bd](https://doi.org/10.3847/1538-4357/ab94bd)
- Harikane, Y., Ouchi, M., Oguri, M., et al. 2023, *ApJS*, 265, 5, doi: [10.3847/1538-4365/acaaa9](https://doi.org/10.3847/1538-4365/acaaa9)
- Isobe, Y., Ouchi, M., Suzuki, A., et al. 2022, *ApJ*, 925, 111, doi: [10.3847/1538-4357/ac3509](https://doi.org/10.3847/1538-4357/ac3509)
- Isobe, Y., Ouchi, M., Tominaga, N., et al. 2023, arXiv e-prints, arXiv:2307.00710, doi: [10.48550/arXiv.2307.00710](https://doi.org/10.48550/arXiv.2307.00710)
- Izotov, Y. I., Thuan, T. X., & Guseva, N. G. 2012, *A&A*, 546, A122, doi: [10.1051/0004-6361/201219733](https://doi.org/10.1051/0004-6361/201219733)
- Jacob, R., Schönberner, D., & Steffen, M. 2013, *A&A*, 558, A78, doi: [10.1051/0004-6361/201321532](https://doi.org/10.1051/0004-6361/201321532)
- Jiang, F., Dekel, A., Freundlich, J., et al. 2019, *MNRAS*, 487, 5272, doi: [10.1093/mnras/stz1499](https://doi.org/10.1093/mnras/stz1499)
- Jiang, L., Kashikawa, N., Wang, S., et al. 2021, *Nature Astronomy*, 5, 256, doi: [10.1038/s41550-020-01275-y](https://doi.org/10.1038/s41550-020-01275-y)
- Johnson, B. D., Leja, J., Conroy, C., & Speagle, J. S. 2021, *ApJS*, 254, 22, doi: [10.3847/1538-4365/abef67](https://doi.org/10.3847/1538-4365/abef67)
- Kaasinen, M., Bian, F., Groves, B., Kewley, L. J., & Gupta, A. 2017, *MNRAS*, 465, 3220, doi: [10.1093/mnras/stw2827](https://doi.org/10.1093/mnras/stw2827)
- Kashino, D., & Inoue, A. K. 2019, *MNRAS*, 486, 1053, doi: [10.1093/mnras/stz881](https://doi.org/10.1093/mnras/stz881)

- Kashino, D., Silverman, J. D., Sanders, D., et al. 2017, *ApJ*, 835, 88, doi: [10.3847/1538-4357/835/1/88](https://doi.org/10.3847/1538-4357/835/1/88)
- Kennicutt, R. C. 1998, *ARA&A*, 36, 189, doi: [10.1146/annurev.astro.36.1.189](https://doi.org/10.1146/annurev.astro.36.1.189)
- Kewley, L. J., & Dopita, M. A. 2002, *ApJS*, 142, 35, doi: [10.1086/341326](https://doi.org/10.1086/341326)
- Kewley, L. J., Nicholls, D. C., Sutherland, R., et al. 2019, *ApJ*, 880, 16, doi: [10.3847/1538-4357/ab16ed](https://doi.org/10.3847/1538-4357/ab16ed)
- Killi, M., Watson, D., Fujimoto, S., et al. 2023, *MNRAS*, 521, 2526, doi: [10.1093/mnras/stad687](https://doi.org/10.1093/mnras/stad687)
- Kojima, T., Ouchi, M., Rauch, M., et al. 2020, *ApJ*, 898, 142, doi: [10.3847/1538-4357/aba047](https://doi.org/10.3847/1538-4357/aba047)
- Luridiana, V., Morisset, C., & Shaw, R. A. 2015, *A&A*, 573, A42, doi: [10.1051/0004-6361/201323152](https://doi.org/10.1051/0004-6361/201323152)
- Madau, P., & Dickinson, M. 2014, *ARA&A*, 52, 415, doi: [10.1146/annurev-astro-081811-125615](https://doi.org/10.1146/annurev-astro-081811-125615)
- Matsumoto, A., Ouchi, M., Nakajima, K., et al. 2022, *ApJ*, 941, 167, doi: [10.3847/1538-4357/ac9ea1](https://doi.org/10.3847/1538-4357/ac9ea1)
- Mo, H. J., & White, S. D. M. 2002, *MNRAS*, 336, 112, doi: [10.1046/j.1365-8711.2002.05723.x](https://doi.org/10.1046/j.1365-8711.2002.05723.x)
- Nagao, T., Maiolino, R., De Breuck, C., et al. 2012, *A&A*, 542, L34, doi: [10.1051/0004-6361/201219518](https://doi.org/10.1051/0004-6361/201219518)
- Nakajima, K., & Ouchi, M. 2014, *MNRAS*, 442, 900, doi: [10.1093/mnras/stu902](https://doi.org/10.1093/mnras/stu902)
- Nakajima, K., Ouchi, M., Isobe, Y., et al. 2023, arXiv e-prints, arXiv:2301.12825, doi: [10.48550/arXiv.2301.12825](https://doi.org/10.48550/arXiv.2301.12825)
- Nakajima, K., Ouchi, M., Xu, Y., et al. 2022, *ApJS*, 262, 3, doi: [10.3847/1538-4365/ac7710](https://doi.org/10.3847/1538-4365/ac7710)
- Oguri, M. 2010, *PASJ*, 62, 1017, doi: [10.1093/pasj/62.4.1017](https://doi.org/10.1093/pasj/62.4.1017)
- Ono, Y., Harikane, Y., Ouchi, M., et al. 2023, *ApJ*, 951, 72, doi: [10.3847/1538-4357/acd44a](https://doi.org/10.3847/1538-4357/acd44a)
- Pontoppidan, K. M., Barrientes, J., Blome, C., et al. 2022, *ApJL*, 936, L14, doi: [10.3847/2041-8213/ac8a4e](https://doi.org/10.3847/2041-8213/ac8a4e)
- Salpeter, E. E. 1955, *ApJ*, 121, 161, doi: [10.1086/145971](https://doi.org/10.1086/145971)
- Sanders, R. L., Shapley, A. E., Kriek, M., et al. 2016a, *ApJ*, 816, 23, doi: [10.3847/0004-637X/816/1/23](https://doi.org/10.3847/0004-637X/816/1/23)
- . 2016b, *ApJL*, 825, L23, doi: [10.3847/2041-8205/825/2/L23](https://doi.org/10.3847/2041-8205/825/2/L23)
- Santini, P., Fontana, A., Castellano, M., et al. 2017, *ApJ*, 847, 76, doi: [10.3847/1538-4357/aa8874](https://doi.org/10.3847/1538-4357/aa8874)
- Schaerer, D., Izotov, Y. I., Nakajima, K., et al. 2018, *A&A*, 616, L14, doi: [10.1051/0004-6361/201833823](https://doi.org/10.1051/0004-6361/201833823)
- Shibuya, T., Ouchi, M., & Harikane, Y. 2015, *ApJS*, 219, doi: [10.1088/0067-0049/219/2/15](https://doi.org/10.1088/0067-0049/219/2/15)
- Shimakawa, R., Kodama, T., Steidel, C. C., et al. 2015, *MNRAS*, 451, 1284, doi: [10.1093/mnras/stv915](https://doi.org/10.1093/mnras/stv915)
- Song, M., Finkelstein, S. L., Ashby, M. L. N., et al. 2016, *ApJ*, 825, 5, doi: [10.3847/0004-637X/825/1/5](https://doi.org/10.3847/0004-637X/825/1/5)
- Speagle, J. S., Steinhardt, C. L., Capak, P. L., & Silverman, J. D. 2014, *ApJS*, 214, 15, doi: [10.1088/0067-0049/214/2/15](https://doi.org/10.1088/0067-0049/214/2/15)
- Stefanon, M., Bouwens, R. J., Labbé, I., et al. 2017, *ApJ*, 843, 36, doi: [10.3847/1538-4357/aa72d8](https://doi.org/10.3847/1538-4357/aa72d8)
- Steidel, C. C., Strom, A. L., Pettini, M., et al. 2016, *ApJ*, 826, 159, doi: [10.3847/0004-637X/826/2/159](https://doi.org/10.3847/0004-637X/826/2/159)
- Steidel, C. C., Rudie, G. C., Strom, A. L., et al. 2014, *ApJ*, 795, 165, doi: [10.1088/0004-637X/795/2/165](https://doi.org/10.1088/0004-637X/795/2/165)
- Storey, P. J., & Zeippen, C. J. 2000, *MNRAS*, 312, 813, doi: [10.1046/j.1365-8711.2000.03184.x](https://doi.org/10.1046/j.1365-8711.2000.03184.x)
- Swinbank, A. M., Harrison, C. M., Tiley, A. L., et al. 2019, *MNRAS*, 487, 381, doi: [10.1093/mnras/stz1275](https://doi.org/10.1093/mnras/stz1275)
- The Astropy Collaboration. 2018, *astropy v3.1: a core python package for astronomy*, 3.1, Zenodo, Zenodo, doi: [10.5281/zenodo.4080996](https://doi.org/10.5281/zenodo.4080996)
- Treu, T., Roberts-Borsani, G., Bradac, M., et al. 2022, *ApJ*, 935, 110, doi: [10.3847/1538-4357/ac8158](https://doi.org/10.3847/1538-4357/ac8158)
- Umeda, H., Ouchi, M., Nakajima, K., et al. 2022, *ApJ*, 930, 37, doi: [10.3847/1538-4357/ac602d](https://doi.org/10.3847/1538-4357/ac602d)